Nature Environment and Pollution Technology
An International Quarterly Scientific Journal

p-ISSN: 0972-6268
(Print copies up to 2016)
e-ISSN: 2395-3454

Vol. 25 | No. 3 | Article ID B4401 | 2026

Original Research Paper

https://doi.org/10.46488/NEPT.2026.v25i03.B4401

Open Access Journal

Characterization and Optimization of *Tamarindus indica* Copper Nanoparticles (TA-CuNPs) for the Adsorptive Removal of Malachite Green

Pampana Anil Kumar[1], Alpitha Suhasini J.[2], Sarva Rao B.[3], Pulipati King[1], D. Appala Naidu[1] and Meena Vangalapati[1]†

[1]Department of Chemical Engineering, AUCE, Visakhapatnam, A.P, India
[2]Department of Chemical & Petroleum Engineering, UCEK, JNTUK, Kakinada, A.P, India
[3]Department of Chemical Engineering, MVGR, Vizianagaram, A.P, India
†Corresponding author: Meena Vangalapati; meenasekhar2002@yahoo.com

Abbreviation: Nat. Env. & Poll. Technol.
Website: www.neptjournal.com

Received: 09-10-2025
Revised: 03-12-2025
Accepted: 15-12-2025

Key Words:

Malachite Green
TA-CuNPs
Adsorption
Green synthesis
RSM-CCD

Citation for the Paper:

Pampana, A.K., Alpitha, S.J., Sarva, R.B., Pulipati, K., Appala Naidu, D. and Vangalapati, M., 2026. Characterization and optimization of Tamarindus indica copper nanoparticles (Ta-Cunps) for the adsorptive removal of malachite green. *Nature Environment and Pollution Technology*, 25(3), B4401. https://doi.org/10.46488/NEPT.2026.v25i03.B4401

Note: From 2025, the journal has adopted the use of Article IDs in citations instead of traditional consecutive page numbers. Each article is now given individual page ranges starting from page 1.

ABSTRACT

Copper nanoparticles doped with *Tamarindus indica* seed extract (TA-CuNPs) were green-synthesized to combine sustainability with an enhanced adsorption potential for wastewater treatment. Comprehensive characterization (SEM, FTIR, XRD, and BET) confirmed the porous structure and active surface functionalities of the materials. Batch adsorption studies of Malachite Green (MG) demonstrated a strong dependence on solution pH, adsorbent dosage, dye concentration, contact time, and temperature, with optimal performance at pH 6 and 0.5 $g.L^{-1}$. The Langmuir isotherm provided the best equilibrium fit (R^2 = 0.999), yielding a monolayer capacity of 243.90 $mg.g^{-1}$. Kinetic evaluation confirmed pseudo-second-order dominance (R^2 = 0.999), indicating chemisorption, while thermodynamic analysis revealed spontaneous and endothermic uptake ($\Delta G° < 0$, $\Delta H° > 0$). RSM-CCD optimization identified the ideal operational conditions: 19.85 $mg.L^{-1}$ MG, 0.498 $g.L^{-1}$ adsorbent, pH 6.18, and 318 K, achieving maximum removal efficiency with excellent model accuracy (R^2 > 0.98, low error statistics). These results collectively establish TA-CuNPs as a high-capacity, green-synthesized, and scalable adsorbent suitable for practical wastewater treatment.

1. INTRODUCTION

Synthetic dyes are major aquatic pollutants owing to the rapid expansion of the textile industry, which has increased the discharge of wastewater contaminated by dyes. Strong structural stability and resistance to degradation are characteristics of Malachite Green (MG), a highly persistent cationic dye used extensively in textiles, aquaculture, food processing, and disinfectants. Due to its environmental persistence, it can bioaccumulate and cause carcinogenic, mutagenic, and reproductive toxicity in humans and aquatic organisms (Chowdhury et al. 2011, Agarwal et al. 2016, Hussien Hamad 2023).

Although many remediation methods have been investigated, including photocatalysis, oxidation, membrane filtration, and biological treatments, many of them have high operating costs, produce sludge, or are ineffective against stable dyes. Owing to its simplicity, low cost, and high efficiency, adsorption remains the most reliable and cost-effective method for eliminating persistent organic contaminants (Jain et al. 2007).

A variety of nanomaterials have demonstrated strong adsorption potential, including ZnS–Cu/AC composites (Dastkhoon et al. 2015), iron-loaded ash (Agarwal et al. 2016), pomegranate-peel-supported zero-valent iron nanoparticles (Gündüz & Bayrak 2018), cellulose–Ag nanofibers (Nagalakshmi et al. 2021), and modified bentonite (Bishwas et al. 2023), etc., etc. Their high surface area, reactivity, and tunable surface chemistry make nanomaterials appealing adsorbents;

however, challenges remain regarding synthesis cost, environmental safety, and scalability.

Green synthesis has emerged as a sustainable alternative to conventional chemical routes, utilizing plant extracts as natural reducing and stabilizing agents to eliminate toxic reagents (Nadagouda et al. 2010, Shahwan et al. 2011). Recent plant-mediated syntheses, including *Hibiscus rosa-sinensis* (Au, Ag) (Philip 2010), *Sorghum* bran (Fe, Ag) (Njagi 2011), *Terminalia chebula* (Pd, Fe) (Kumar et al. 2013), and *Grevillea robusta* (Ag) (Poiba et al. 2023), etc., demonstrate the feasibility, biocompatibility, and environmental safety of these approaches. Coupled with low-cost techniques such as co-precipitation, green nanomaterials offer promising pathways for sustainable wastewater treatment (Bashanaini 2019, Sowjanya et al. 2023).

No previous study has reported the synthesis of TA-CuNPs using *Tamarindus indica* seed extract for MG removal or evaluated their adsorption behavior using integrated kinetic, thermodynamic, and RSM-CCD optimization. This study investigated the influence of pH, initial dye concentration, adsorbent dosage, contact time, and temperature on MG removal, evaluated adsorption kinetics, isotherms, and thermodynamics, and applied RSM-CCD to optimize the process conditions. This study contributes to sustainable wastewater treatment by demonstrating a low-cost, bio-derived nanomaterial with high adsorption efficiency and strong potential for scale-up.

2. MATERIALS AND METHODS

2.1. Production of *Tamarindus indica* Seed-Doped Copper Nanoparticles (TA-CuNPs)

To ensure a high availability of phytochemicals that may serve as reductants and capping agents, a concentrated *Tamarindus indica* seed extract was prepared. Since concentrated plant extracts were proven for rapid metal-ion reduction during the synthesis of green nanoparticles, the high solid–liquid ratio was intentionally employed. Specifically, 50 g of ground seed powder was suspended in 250 mL of distilled water and heated to 80°C for 60 min using a hot-plate heater equipped with magnetic stirring. To get a clarified extract, the mixture was filtered. In order to create nanoparticles, 5 mL of the extract was added dropwise to 50 mL of a newly made 0.005 M $CuSO_4 \cdot 2H_2O$ solution while being continuously stirred at an ambient temperature. The reaction was allowed to proceed for 30 min, during which the transition from a light to a dark brown coloration provided qualitative confirmation of Cu^{2+} reduction and nanoparticle formation. The suspension was subsequently centrifuged at 4250 rpm for 30 min to recover the solid phase. After being dried for 12 h at 373 K in a hot-air oven, the separated material was carefully ground into a uniform powder. Since the study used a low-temperature green synthesis method to preserve phytochemical functional groups, no calcination was carried out. Before characterization and adsorption tests, the finished product was kept in airtight containers under carefully regulated laboratory conditions (25 ± 2 °C, low ambient humidity).

2.2. Batch Adsorption Experiments

Under experimental conditions, the batch adsorption performance of TA-doped copper nanoparticles (TA-CuNPs) toward malachite green (MG) was methodically examined. Each trial involved adding 0.4 g of TA-CuNPs to 100 mL of MG solution (20–100 $mg.L^{-1}$) in 250 mL Erlenmeyer flasks, which were then shaken at 150 rpm for 5–60 min using a temperature regulated orbital shaker kept at 308 K. Using 0.1 M HCl or NaOH, the pH of the solution was adjusted between 3 and 8, and pH stability was confirmed both before and after each experiment. Every adsorption test was performed in triplicate, and to account for any non-adsorptive losses, the proper blanks (MG solution without adsorbent) were employed.

Following adsorption, the suspensions were centrifuged at 4000 rpm for 15 min, and the supernatant was filtered through 0.45 µm membrane filters prior to analysis. The residual MG concentration was quantified using a UV–Vis spectrophotometer at λ_{max} = 423 nm with a 1 cm quartz cuvette. Adsorption capacity/ dye uptake (q_e) and removal efficiency (%) were calculated using Eqs. (1) and (2) (R K Bishwas et al. 2023, Sowjanya et al. 2023)

$$\% \text{ Adsorption/Removal of dye} = \left(\frac{C_o - C_t}{C_o}\right) \times 100 \quad \ldots(1)$$

$$\text{Adsorption capacity/Dye uptake } q_t = \left(\frac{C_o - C_t}{m^*}\right) \times V \quad \ldots(2)$$

Where V (in L) is the solution's volume, m^* (in g) is the adsorbent's mass, and C_o and C_t (in $mg.L^{-1}$) show the initial and equilibrium MG dye concentrations. The adsorption mechanism was then clarified by using these experimental results for kinetic, isotherm, and thermodynamic modeling.

2.3. Kinetic, Equilibrium, and Thermodynamic Analyses of MG Adsorption

Employing pseudo-first-order and pseudo-second-order models, the adsorption kinetics of Malachite Green (MG) onto TA–Cu-NPs were assessed to elucidate the rate-governing mechanism. In the pseudo-first-order model, adsorption is described by the difference between the uptake

at time t (q_t) and the equilibrium uptake (q_e), where the q_e values were experimentally determined from independent equilibrium adsorption trials conducted under identical conditions (Dastkhoon et al. 2015). The pseudo-second-order model attributes the rate to chemisorption, which involves electron sharing or transfer between MG molecules and the functional groups present on the nanoparticle surface (Mortazavi et al. 2016). All kinetic parameters were obtained using nonlinear regression, as this approach minimizes the systematic errors associated with linear transformations and provides more robust fits to the experimental data. To find the best kinetic representation, both models were evaluated using the statistical indices R^2, RMSE, and χ^2.

The equation of Pseudo-first-order kinetics:

$$\ln(q_e - q_t) = \ln q_e - k_1 t \quad \ldots(3)$$

The equation of Pseudo-second-order kinetics:

$$\frac{t}{q_t} = \frac{1}{k_2 q_e^{\,2}} + \frac{t}{q_m} \quad \ldots(4)$$

Here, t is the time, representing the adsorption time, while the pseudo-first-order and pseudo-second-order rate constants are indicated by k_1 and k_2, respectively.

Using the Langmuir and the Freundlich isotherm models, the equilibrium uptake of MG onto the TA-Cu NPs was evaluated at 318 K to determine the monolayer adsorption capacity and characterize the surface heterogeneity of the nanoparticles. The Freundlich model is more applicable in nonideal situations because it allows adsorption on heterogeneous surfaces with variable energies. In contrast, the Langmuir model presupposes monolayer adsorption on a homogeneous surface with a limited number of identical sites (Jain et al. 2007).

The expression for the Langmuir model: $q_e = \frac{q_{\max} K_L C_e}{1 + K_L C_e}$ …(5)

Where: q_e (in $mg.g^{-1}$) is the adsorption capacity at equilibrium condition, C_e (in $mg.L^{-1}$) is the dye concentration at equilibrium, q_{max} (in $mg.g^{-1}$) is the highest monolayer adsorption capacity, and K_L (in $L.mg^{-1}$) denotes the adsorption constant of Langmuir, and it reflects the affinity of the adsorbent & adsorbate.

The equation for the Freundlich model is written as:

$$q_e = K_f C_e^{\,1/n} \quad \ldots(6)$$

Where: "K_f" $(mg.g^{-1}).(mg.L^{-1})^{-n}$ represents the constant of the Freundlich, it indicates the adsorption capacity, and "n" stands for the heterogeneity factor, which provides insight into the intensity of adsorption and adsorbent surface irregularity.

The key thermodynamic parameters, namely change in Gibbs free energy (ΔG°), enthalpy change (ΔH°), and change in entropy (ΔS°), were measured over the temperature range of 303–318 K to clarify the characteristics and feasibility of the adsorption process. To comprehend the system's spontaneity and energetic characteristics, the dimensionless equilibrium constant ($K_c = q_e/C_e$) was calculated by dividing the dye's equilibrium concentration in the solution by the amount adsorbed on the nanoparticles, providing the basis for evaluating ΔG° and related thermodynamic behavior. Using the following relationship, the standard free energy change was calculated:

$$\Delta G^o = -RT \ln(K_c) \quad \ldots(7)$$

Where: T (in K) is the absolute temperature and R (in 8.314 $J.moL^{-1}.K^{-1}$) is the universal gas constant. The following linearized form of expression was used to estimate the values of ΔS° and ΔH° from the intercept and slope of the Van't Hoff plot.

$$\ln Kc = \frac{\Delta S^o}{R} - \frac{\Delta H^o}{RT} \quad \ldots(8)$$

This analysis shed light on the disorder, heat changes, and spontaneity related to MG adsorption onto TA-Cu-NPs.

2.4. Response Surface Methodology (RSM)

The Central Composite Design (CCD), a widely used Response Surface Methodology (RSM) tool, enables efficient process optimization by capturing linear, interaction, and quadratic effects with a minimal number of experimental trials (Jain et al. 2007, Agarwal et al. 2016). In this study, a rotatable CCD was implemented, consisting of 30 experimental runs, integrating factorial, axial ("star"), and center points to ensure uniform prediction accuracy across the design space (Sowjanya et al. 2023). The optimization focused on four independent variables: initial MG dye

Table 1: Matrix for a 2-factor Central Composite Design (CCD).

Factor	Name	Units	Lower Limit	Upper Limit	Coded Low	Coded High
A	Concentration, C_o	$mg.L^{-1}$	10.0	30.0	-1 ↔ 15.0	+1 ↔ 25.0
B	Dosage of adsorbent, w	$g.L^{-1}$	0.3	0.7	-1 ↔ 0.4	+1 ↔ 0.6
C	Solution pH		4.0	8.0	-1 ↔ 5.0	+1 ↔ 7.0
D	Temperature, T	K	308.0	328.0	-1 ↔ 313.0	+1 ↔ 323.0

concentration (A, mg.L^{-1}), adsorbent dosage (B, g), solution pH (C), and temperature (D, K), modeled using a second-order quadratic polynomial in Design-Expert v13, with the full CCD matrix presented in Table 1. The adsorption performance was quantified as the percentage removal of MG. ANOVA was used to confirm the model adequacy; significant model terms and an insignificant lack of fit indicated strong predictive performance. The dependability of the response surface model was supported by diagnostic tests that confirmed normality, constant variance, and the lack of significant outliers. These tests included residual plots and normal probabilities.

2.5. Characterization of TA-Doped Cu Nanoparticles

The structural and surface characteristics of the copper nanoparticles doped with the TA seed extract were carefully examined using XRD, SEM, FTIR, and BET. The XRD pattern of the TA–CuNPs shown in Fig. 1 exhibits broad, low-intensity features characteristic of nanostructured copper-based materials, with the principal reflections appearing at $2\theta \approx 21.96^{\circ}$, 22.88°, 28.11°, and 35.86°, the latter showing the highest relative intensity. Although the pattern lacks the sharp, well-defined peaks typical of bulk FCC Cu, the observed maxima near 35.8° and 41.5° may be attributed to mixed copper oxide phases most closely resembling CuO/Cu_2O signatures rather than metallic Cu, given the lack of reflections matching the standard Cu (JCPDS 04-0836). The strong background scattering and broadening of all peaks (FWHM $0.33–0.60^{\circ}$) further suggest highly dispersed, well-crystallized nanoparticles, which is consistent with synthesis mediated by phytochemicals. The SEM images (Fig. 2a, b) depict chiefly spherical, porous particulates with an approximate mean size of 500 nm, an architecture conducive to enhanced adsorption. For full analytical transparency, the image should present scale bars alongside the operating conditions, such as an accelerating voltage of 15.0 kV and a working distance of 10.24 mm. Together, these findings show that TA–CuNPs have a high surface area and crystallographic stability required for effective dye adsorption. The FTIR spectra of TA–CuNPs before and after MG adsorption,

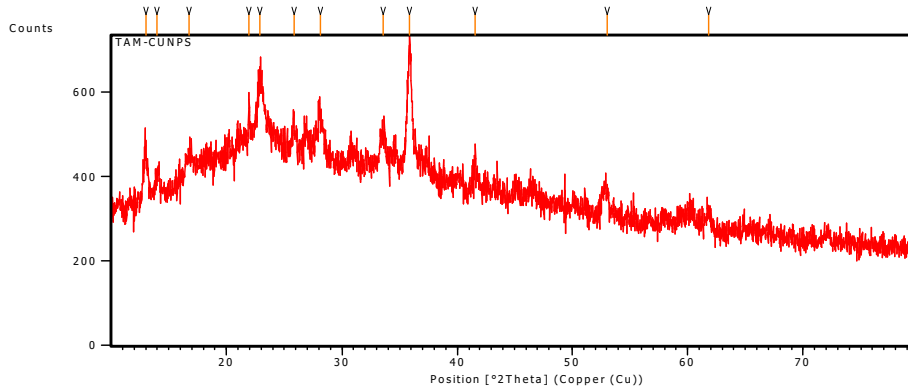

Fig. 1: Xray diffraction (XRD) pattern of TACuNPs.

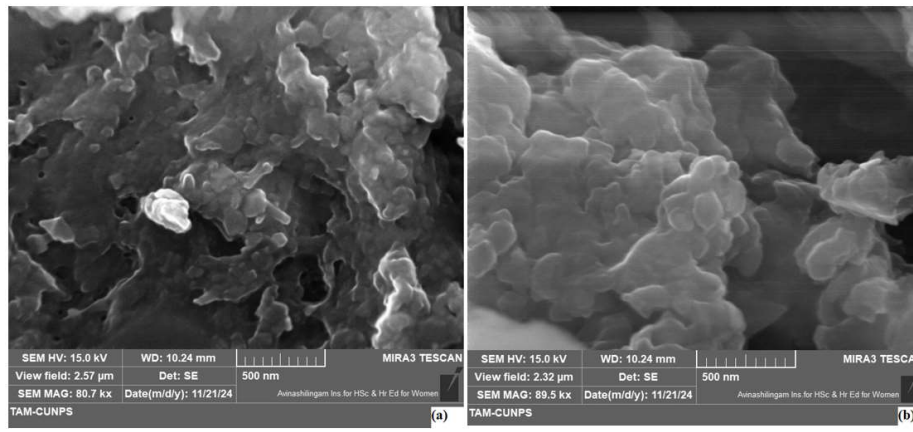

Fig. 2: Scanning Electron Microscope (SEM) image of TA-CuNPs.

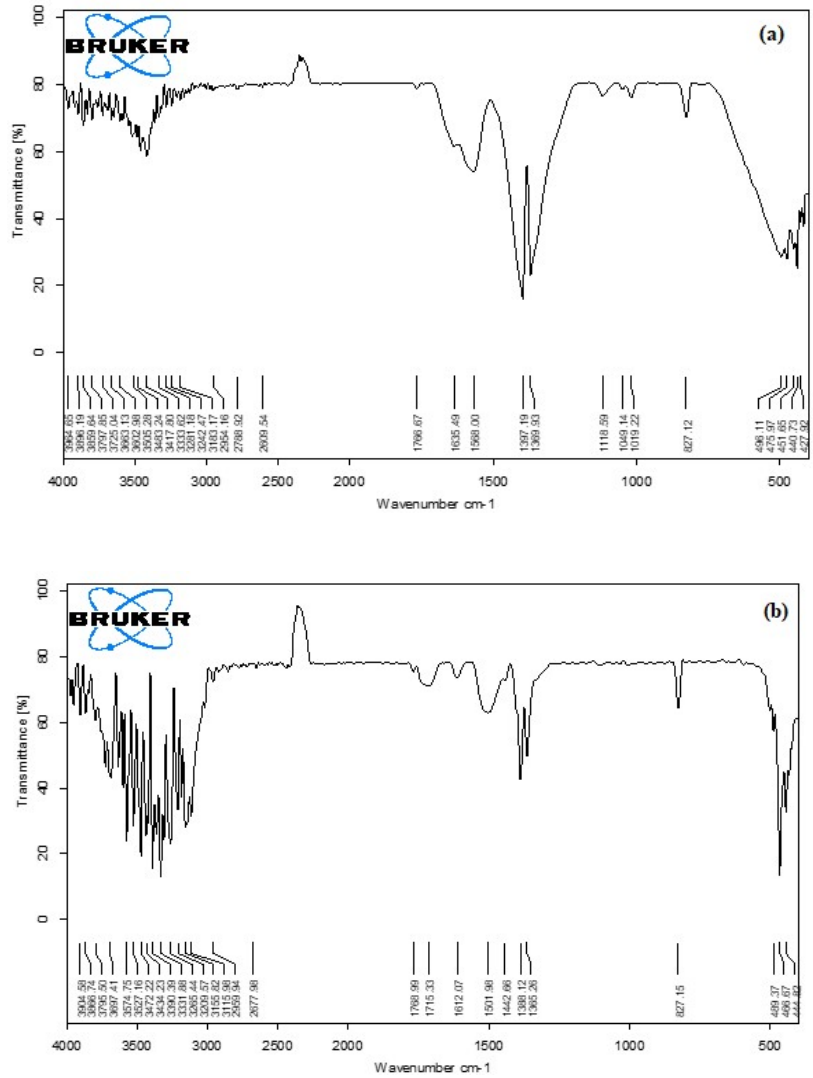

Fig. 3: (a & b). FTIR spectrum of TA–CuNPs adsorbent before & after MG adsorption.

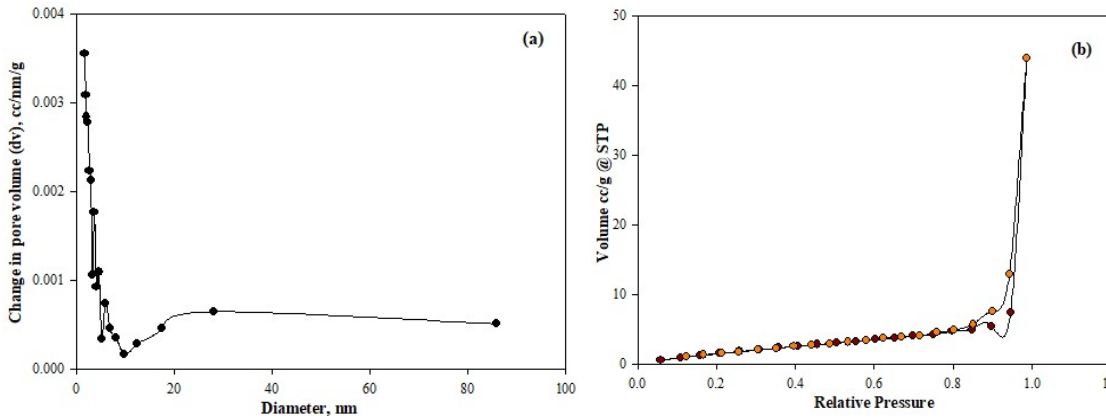

Fig. 4: (a). BET pore size distribution, (b). BET plot of the N_2 adsorption-desorption isotherm.

presented in Fig. 3a and b, exhibit modest but distinct shifts in the O–H/N–H stretching region from 3483 to 3472 cm^{-1} and C–N/C–O region from 1397 to 1388 cm^{-1}, indicating the participation of surface hydroxyl and amine groups in dye binding. These trends are consistent with those of earlier reports on phytochemical-capped metal nanoparticles (Eid et al. 2023, Ejeta et al. 2024). Spectra were recorded from 4000–400 cm^{-1} at 4 cm^{-1} resolution, enabling the reliable identification of adsorption-induced vibrational changes. These findings align with the well-established role of FTIR in elucidating surface alterations and functional group involvement during adsorption in systems of green-synthesized nanoparticles. The pore volume of the adsorbent and surface area of the TA-CuNPs were analyzed using a surface area analyzer. BET nitrogen adsorption analysis at 77 K confirmed a microporous structure (pore diameter 1.795 nm) with a surface area of 15.259 $m^2.g^{-1}$ and pore volume of 0.073 $cm^3.g^{-1}$, while Fig. 4a, b presents the corresponding pore-size distribution and N_2 adsorption–desorption isotherms.

3. RESULTS AND DISCUSSION

3.1. Contact Time Effect on MG Adsorption

The effects of MG adsorption on TACuNPs were investigated for 5–60 min at pH 6, 308 K, 100 $mg.L^{-1}$, and 0.4 $g.L^{-1}$ dosage. A sharp initial uptake was observed, with the system reaching equilibrium at approximately 40 min, as shown in Fig. 5a. This rapid early stage is attributed to the abundance of readily accessible active sites and dominant film diffusion, which facilitate fast dye transfer to the nanoparticle surface. The plateau at 40 min indicates a shift in the rate-controlling mechanism: as the surface sites become progressively occupied, intraparticle (pore) diffusion becomes the limiting step, slowing further adsorption. Thus, the equilibrium time reflects the combined effect of surface site saturation and the transition from rapid film diffusion to slower pore diffusion. This trend demonstrates the strong adsorption capacity and efficient kinetics of TA-CuNPs, which are comparable to those of other advanced nanocomposite adsorbents.

3.2. Adsorbent Dosage's Effect on MG Removal

The MG removal efficiency of TACuNPs increased from 89.7% to 91.4% as the dosage was increased from 0.1 to 0.8 $g.L^{-1}$ under fixed conditions (40 min, pH 6.8, 100 $mg.L^{-1}$ MG, and 308 K). However, the efficiency plateau observed beyond 0.5 $g.L^{-1}$ (Fig. 5b) indicates that the additional adsorbent no longer enhances performance. At higher concentrations, the nanoparticles tend to agglomerate, leading to overlapping active sites and a reduction in the accessible surface area. Additionally, this aggregation creates a screening effect that decreases the number of effective adsorption sites and restricts dye diffusion toward the inner pores. Recent studies on nanocomposite adsorbents, such as copper ferrite/calcium alginate nanocomposites (Hassan et al. 2024) and bio-fabricated CuO nanoparticles (Ejeta et al. 2024) used for MG removal, showed dosage-dependent saturation behavior, where excessive adsorbent mass resulted in diminished surface availability and diffusion limitations.

3.3. Effect of Solution pH on MG Adsorption

The pH strongly affected the MG adsorption by regulating both the dye ionization and surface charge of the TA-CuNPs. Experiments conducted at pH 3–8 (308 K, 100 $mg.L^{-1}$ MG, 50 min) showed maximum removal at pH 6, as shown in Fig. 5c. At this pH, the zeta potential of the TA-CuNPs became sufficiently negative, promoting a strong electrostatic attraction to cationic MG. The proton competition for active sites causes reduced adsorption at pH < 6, whereas excess negative charge at higher pH probably causes electrostatic repulsion and restricts uptake. Thus, pH 6 was selected as the optimum value for further experiments.

3.4. Effect of Initial Dye Concentration on MG Adsorption

The effects of initial MG concentration (20–100 $mg.L^{-1}$) on adsorption by TA-CuNPs were evaluated under experimental conditions (pH 6, 308 K, 40 min). The percentage removal decreased as the dye concentration increased (Fig. 5d). At low concentrations, the high concentration gradient provides a strong driving force for mass transfer, allowing MG molecules to be efficiently captured by available active sites. However, with increasing concentration, these sites rapidly become occupied, and the driving force is no longer sufficient to overcome site saturation. This behavior is consistent with Langmuir monolayer adsorption, in which the removal efficiency decreases at high MG concentrations as the surface approaches its maximum loading capacity.

3.5. Kinetic Study of MG Adsorption on TACuNPs

The pseudo-second-order (PSO) model best described the adsorption kinetics of malachite green onto the TA-CuNPs under optimal conditions (pH 6, 318 K, 0.5 $g.L^{-1}$ adsorbent, 100 $mg.L^{-1}$ MG). The PSO model showed an excellent fit, with $R^2 = 0.999$ and close agreement between the calculated and experimental q_e values. Furthermore, a removal efficiency of 92.09% was achieved at an equilibrium time of 40 min, confirming the high adsorption performance of the system. In contrast, the pseudo-first-order model produced higher χ^2 and RMSE values, confirming its poor suitability. The superior performance of the PSO model indicates that

chemisorption is the dominant rate-controlling step, driven by electron sharing or exchange between MG molecules and surface sites on the nanoparticles. This mechanism aligns with the potential coordination interactions between Cu and *Tamarindus indica*-derived functional groups (–OH, –COOH, and phenolic groups). The kinetic parameters are summarized in Table 2, and the kinetic fits are shown in Fig. 6a and b.

3.6. Analysis of Adsorption Isotherms

The adsorption equilibrium of MG on the TA-CuNPs was modeled using the Langmuir and the Freundlich isotherms, as shown in Fig. 7a and b. The Langmuir model showed the strongest agreement with the data ($R^2 = 0.999$), confirming that MG interacts with a uniform surface via monolayer chemisorption. This finding was reinforced by the Langmuir separation factor ($R_L = 0.336$), which remained between 0 and 1, indicating favorable adsorption. The predicted q_{max} (243.902 $mg.g^{-1}$) also closely aligned with the experimental q_e (208.333 $mg.g^{-1}$). Although the Freundlich model ($R^2 = 0.979$) suggests mild surface heterogeneity at higher concentrations, the Langmuir isotherm clearly dominates. The isotherm constants are summarized in Table 3, and Table 4 compares the adsorption performance of TA-CuNPs with that of other reported adsorbents.

3.7. Analysis of Thermodynamics

Using an initial MG concentration of 20 $mg.L^{-1}$, the thermodynamic behavior of adsorption onto TA-CuNPs was examined at 303–318 K. The Van't Hoff plot (ln Kc vs. 1/T) in Fig. 8 shows strong linearity ($R^2 = 0.9903$), allowing ΔH^o and ΔS^o to be calculated from its slope and intercept; the resulting values are listed in Table 5. MG uptake occurred spontaneously at all temperatures under investigation, as confirmed by the consistently negative ΔG° values. A positive ΔH° indicates an endothermic process, which reflects the energy required for MG molecules to overcome hydration forces, reorganize interfacial species, and penetrate the nanoparticle pores. This process may involve minor changes in surface functionalities during binding. Owing to the displacement of structured water molecules and the increased configurational freedom gained as MG occupies adsorption sites on the TA-CuNPs surface, the significantly high ΔS° indicates a marked increase in interfacial disorder. This combined enthalpy–entropy profile explains why adsorption becomes stronger at higher temperatures: the thermal input increases molecular mobility, facilitates removal, and allows for more efficient dye–surface interactions, all of which improve the overall adsorption efficiency.

Table 2: MG's adsorption kinetics onto TA-CuNPs were determined.

Kinetic model	k_1[L. min^{-1}]	k_2, [g.mg^{-1}. min^{-1}]	q_e [$mg.g^{-1}$]	R^2
Pseudo-first-order	0.0956	--	151.836	0.9372
Pseudo-second-order	--	0.00082	208.333	0.9990

Table 3: Adsorption isotherm parameters for MG uptake on TA-CuNPs derived from the model.

Langmuir Isotherm Modeling		Freundlich Isotherm modeling	
b [$L.mg^{-1}$]	0.1017	K_f [$mg^{1-1/n}.L^{1/1}.g^{-1}$]	27.5913
q_{max} [$mg.g^{-1}$]	243.902	n	1.5745
R^2	0.999	R^2	0.979

3.8. Process Optimization Using Response Surface Methodology (RSM)

The "Central Composite Design," consisting of 30 experimental runs, was implemented to optimize the % removal of MG using TA-doped copper nanoparticles

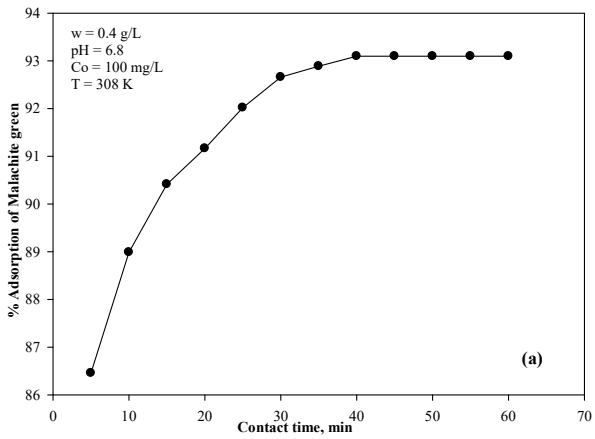

Fig. 5a: Effect of contact time on MG adsorption.

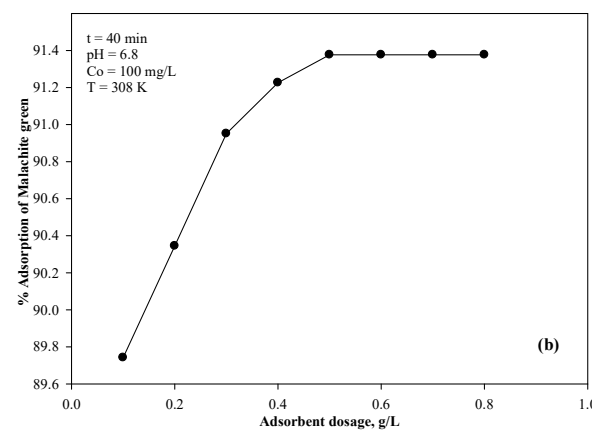

Fig. 5b: Effect of adsorbent dosage on MG adsorption.

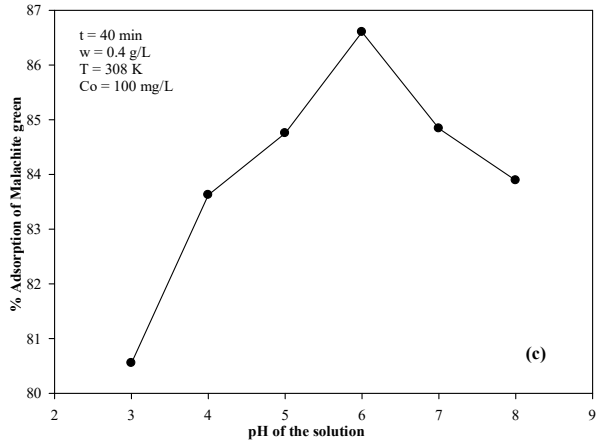

Fig. 5c: Effect of pH on MG adsorption.

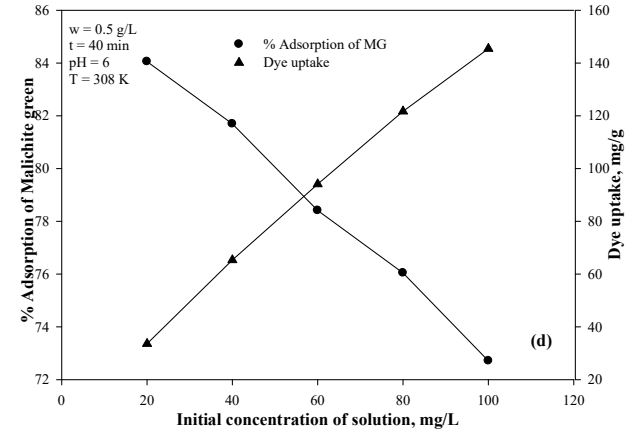

Fig. 5d: Effect of initial dye concentration on MG adsorption.

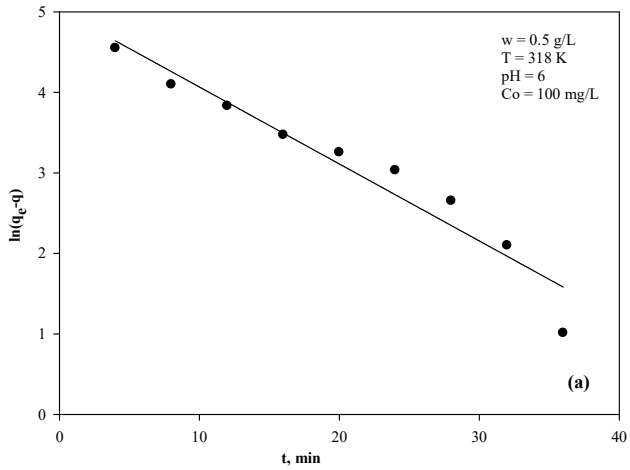

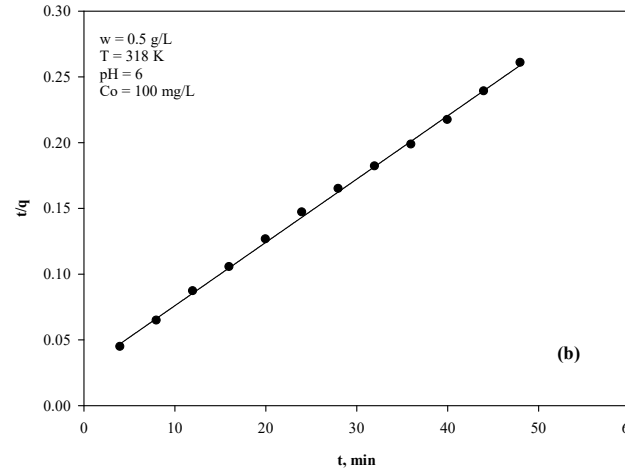

Fig. 6: Kinetic study models for MG adsorption: (a). Pseudo-First-order, (b). Pseudo-Second-order.

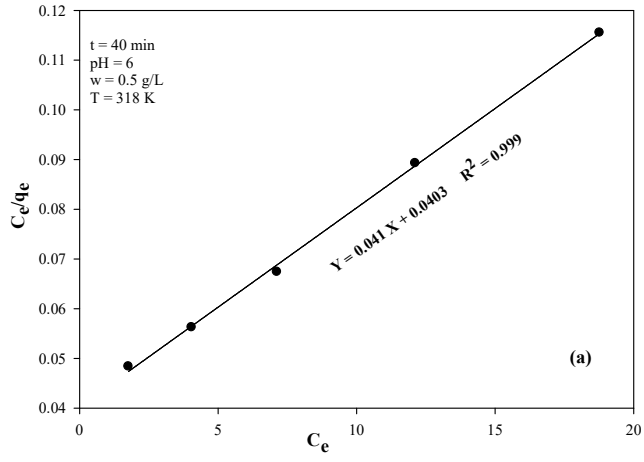

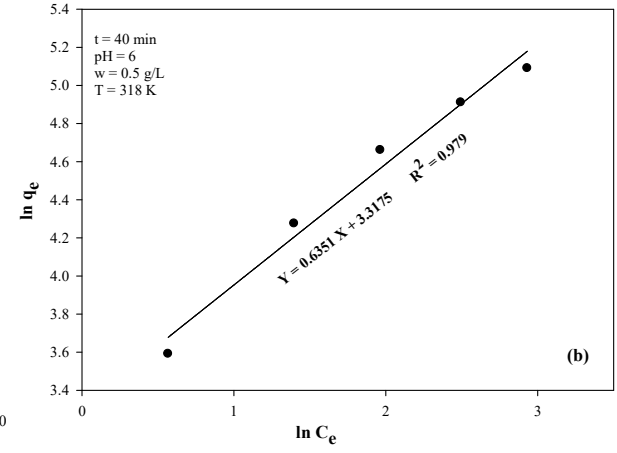

Fig. 7: Adsorption isotherm models for MG adsorption: (a). Langmuir isotherm (b). Freundlich isotherm.

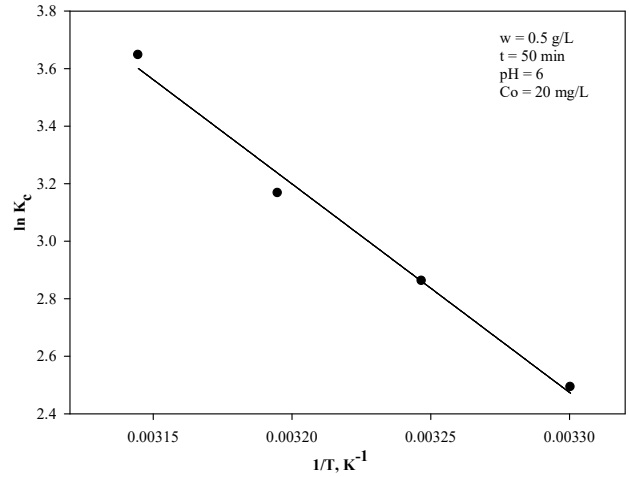

Fig. 8: The thermodynamic evaluation for the adsorption of Malachite green.

Table 4: MG removal from aqueous solution using the relative adsorption capacities of different adsorbents.

S.No.	Type of Adsorbent/Bio-sorbent	Max Dye uptake, $mg.g^{-1}$	Reference
1.	Spent tea leaves-Activated carbon (STAC)	256.40	Akar et al. (2013)
2.	Leaves of the *Solanum tuberosum* potato plant waste	33.33	Gupta et al. (2011)
3.	Pineapple stem	119.05	Hamed et al. (2009)
4.	Dead leaves of *Platanus vulgaris*	85.47	Hamdaouia et al. (2008)
5.	Activated Carbon Supported Zinc Sulfide–Copper Nanocomposite (ZnS–Cu–NP/AC)	168.10	Dastkhoon et al. (2015)
6.	Activated Carbon Supported Silver Nanoparticles (Ag–NP/AC)	95.20	Mortazavi et al. (2016)
7.	Halloysite nanotubes (HNT)	74.95	Turkan and Huseyin (2022)
8.	Cellulose nanofibers and silver nanoparticles	142.00	Chinthalapudi et al. (2021)
9.	TA-doped Cu nanoparticles (TA-CuNPs)	243.90	Present study

Table 5: Thermodynamic variables (ΔG°, ΔH°, and ΔS°) for adsorption of MG onto TA-CuNPs.

Temperature, [K]	Change in Gibbs-Free Energy, ΔG^{o} [$kJ.moL^{-1}$]	Change in Enthalpy, ΔH^{o} [$kJ.moL^{-1}$]	Change in Entropy, ΔS^{o} [$J.moL.K^{-1}$]
308	-6.281	60.295	219.534
313	-7.328		
318	-8.243		
323	-9.628		

(TA-CuNPs). The experimental framework incorporated four independent factors, initial MG dye concentration (A), dosage of adsorbent (B), solution pH (C), and temperature (D), which were systematically varied to investigate both their main effects and interaction influences on the adsorption efficiency. The coded and actual levels of these factors, along with the corresponding experimental responses, are summarized in Table 6. A quadratic (2^{nd}) polynomial regression model was constructed to correlate the % removal of MG with the coded process variables, offering an in-depth depiction of the adsorption behavior under the investigated operational condition.

$$\%Adsorption\ of MG = 91.35 - 0.1688 \times A - 0.3304 \times B + 0.6937 \times C + 0.1729 \times D + 0.1856 \times AB + \ 0.0019 \times AC + 0.4419 \times AC + 0.0806 \times BC + 0.3256 \times BD + 0.2669 \times CD + 3.28 \times A^2 - 3.42 \times B^2 - 3.52 \times C^2 - 2.08 \times D^2 \quad \ldots(9)$$

In the regression analysis, the factors were coded as −1 and +1 to enable a direct comparison of their relative

effects through standardized regression coefficients. With a significant Model F-value of 1755.38 and $p < 0.0001$, the robustness of the quadratic CCD model was confirmed by ANOVA, as shown in Table 7. This indicates that all linear, interaction (AB, AD, BD, and CD), and quadratic terms were statistically significant and that such a large F-value is highly unlikely to arise from noise. Additionally, the model has sufficient predictive power to reliably navigate the experimental design space, as evidenced by the high Adequate Precision of 121.889 and the close alignment of adjusted (0.9988) and predicted (0.9965) R^2 values, which show an excellent signal-to-noise ratio well above the threshold of 4. The optimal conditions were determined to be 19.85 an MG concentration of 0.498 $g.L^{-1}$ adsorbent dosage, pH 6.18, and a temperature of 318.24 K, which were determined through optimization using the desirability function depicted in Fig. 9a. The close match between the experimental and predicted values, as shown in Fig. 9b, further supports the dominance of these interactions and validates the model for reliable process optimization. This resulted in a predicted removal efficiency of 91.37% (desirability = 1.0), a value that is practically relevant for real-world wastewater treatment. Under experimental conditions, an actual removal efficiency of 92.09% was achieved, further validating the reliability and practical applicability of the model. Because of their control over the surface charge and

Table 6: Central Composite Design (CCD) matrix showing the experimental factors and corresponding responses for MG adsorption.

Run	Initial MG Dye Concentration [A]: $mg.L^{-1}$	Adsorbent dosage (B): $g.L^{-1}$	Solution pH [C]:	Temperature [D]: K	Experimental Value	Predicted value
1	15	0.4	5	313	79.86	79.88
2	25	0.4	5	313	78.54	78.38
3	15	0.6	5	313	78.22	78.13
4	25	0.6	5	313	77.43	77.28
5	15	0.4	7	313	80.63	80.67
6	25	0.4	7	313	78.95	79.08
7	15	0.6	7	313	79.35	79.15
8	25	0.6	7	313	78.15	78.30
9	15	0.4	5	323	78.42	78.26
10	25	0.4	5	323	78.21	78.43
11	15	0.6	5	323	77.83	77.71
12	25	0.6	5	323	78.68	78.63
13	15	0.4	7	323	79.85	80.01
14	25	0.4	7	323	80.12	80.19
15	15	0.6	7	323	79.65	79.79
16	25	0.6	7	323	80.82	80.71
17	10	0.5	6	318	78.52	78.31
18	30	0.5	6	318	77.95	77.90
19	20	0.3	6	318	78.52	78.57
20	20	0.7	6	318	76.78	76.99
21	20	0.5	4	318	75.68	75.87
22	20	0.5	8	318	78.84	78.65
23	20	0.5	6	308	82.60	82.68
24	20	0.5	6	328	83.45	83.37
25	20	0.5	6	318	91.35	91.35
26	20	0.5	6	318	91.35	91.35
27	20	0.5	6	318	91.35	91.35
28	20	0.5	6	318	91.35	91.35
29	20	0.5	6	318	91.35	91.35
30	20	0.5	6	318	91.35	91.35

Table 7: ANOVA for the quadratic model to describe MG adsorption onto TA-CuNPs.

Source of Variation	Sum of the Squares [SS]	The Degrees of freedom [df]	The Mean Square [MS]	F-value	p-value	
Model	792.38	14	56.60	1755.38	< 0.0001	significant
A: Initial concentration of the MG dye	0.6834	1	0.6834	21.20	0.0003	
B: Adsorbent dosage	2.62	1	2.62	81.26	< 0.0001	
C: Solution pH	11.55	1	11.55	358.25	< 0.0001	
D: Temperature	0.7176	1	0.7176	22.26	0.0003	
AB	0.5513	1	0.5513	17.10	0.0009	
AC	0.0001	1	0.0001	0.0017	0.9672	
AD	3.12	1	3.12	96.89	< 0.0001	
BC	0.1040	1	0.1040	3.23	0.0927	
BD	1.70	1	1.70	52.62	< 0.0001	
CD	1.14	1	1.14	35.34	< 0.0001	
A^2	294.81	1	294.81	9143.33	< 0.0001	
B^2	321.70	1	321.70	9977.29	< 0.0001	
C^2	340.27	1	340.27	10553.48	< 0.0001	
D^2	118.77	1	118.77	3683.74	< 0.0001	
Residual Error	0.4836	15	0.0322			
Lack of Fit	0.4836	10	0.0484			
Pure Error	0.0000	5	0.0000			
Corrected Total	792.86	29				
Adjusted R^2	0.9988					
Predicted R^2	0.9965					
Adeq Precision	121.8890					

active site availability, the 3D response surfaces and contour plots revealed that pH and adsorbent dosage had the strongest effects. Conversely, interactions involving dosage–pH and dosage–temperature were the most prominent, indicating a synergistic enhancement of the adsorption capacity under conditions favoring electrostatic attraction and endothermic uptake. The strong curvature in surface and Contour plots is presented in Fig. 10a-f and Fig.11a-f.

4. CONCLUSIONS

TA-doped copper nanoparticles (TA-CuNPs) synthesized by co-precipitation were extensively characterized (microscopy,

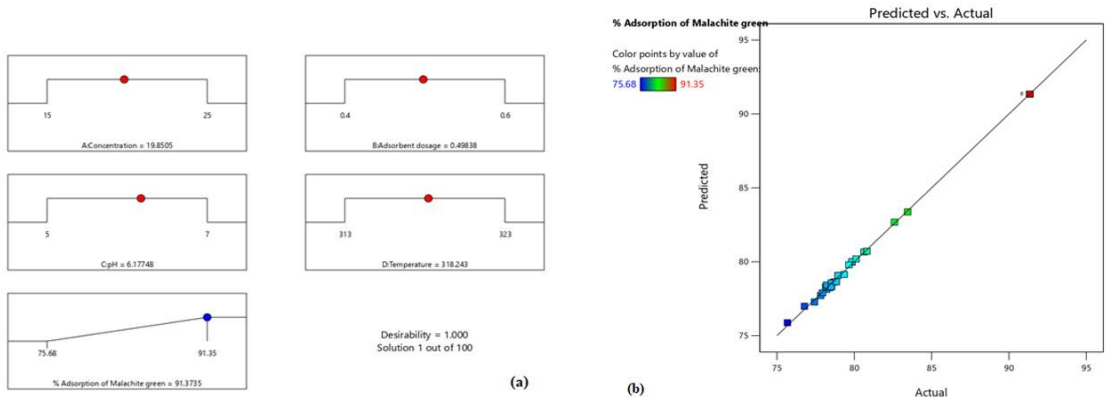

Fig. 9 (a): Ramp plot illustrating the optimized conditions for MG adsorption onto TA-CuNPs, (b). Comparison of the CCD Model's predicted and experimental values.

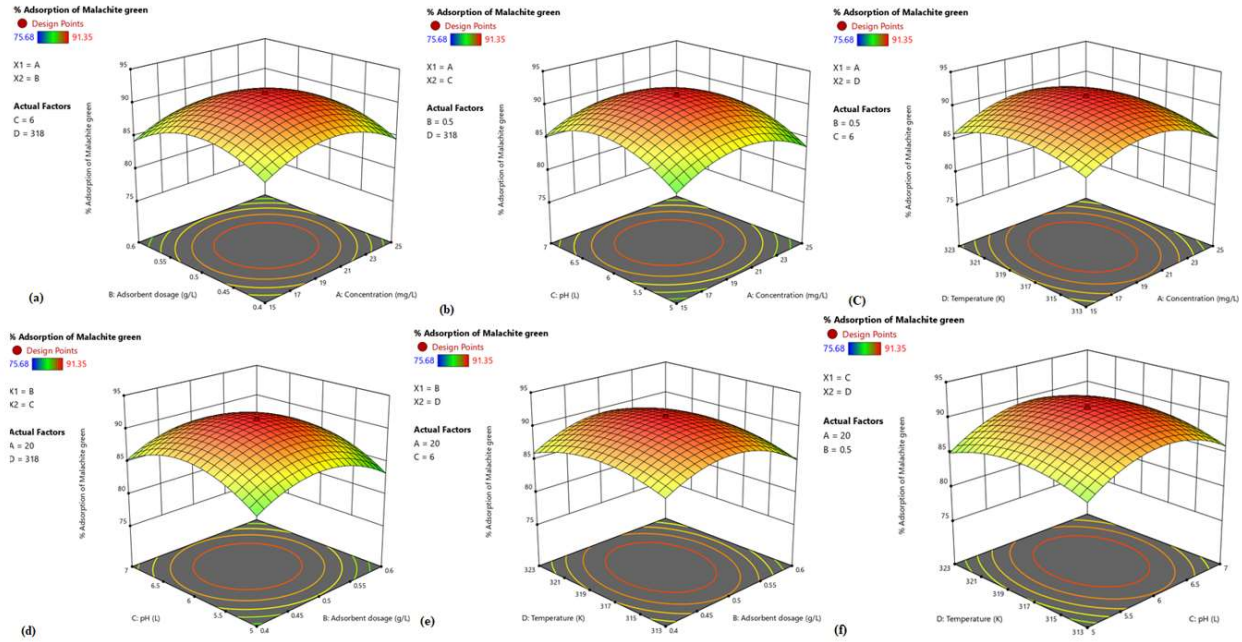

Fig. 10: 3D response-surface plots illustrating the interactive effects of (a) concentration and adsorbent dosage, (b) concentration and pH, (c) concentration and temperature, (d) adsorbent dosage and pH, (e) adsorbent dosage and temperature, (f) pH and temperature on the percentage removal of malachite green by TA-CuNPs.

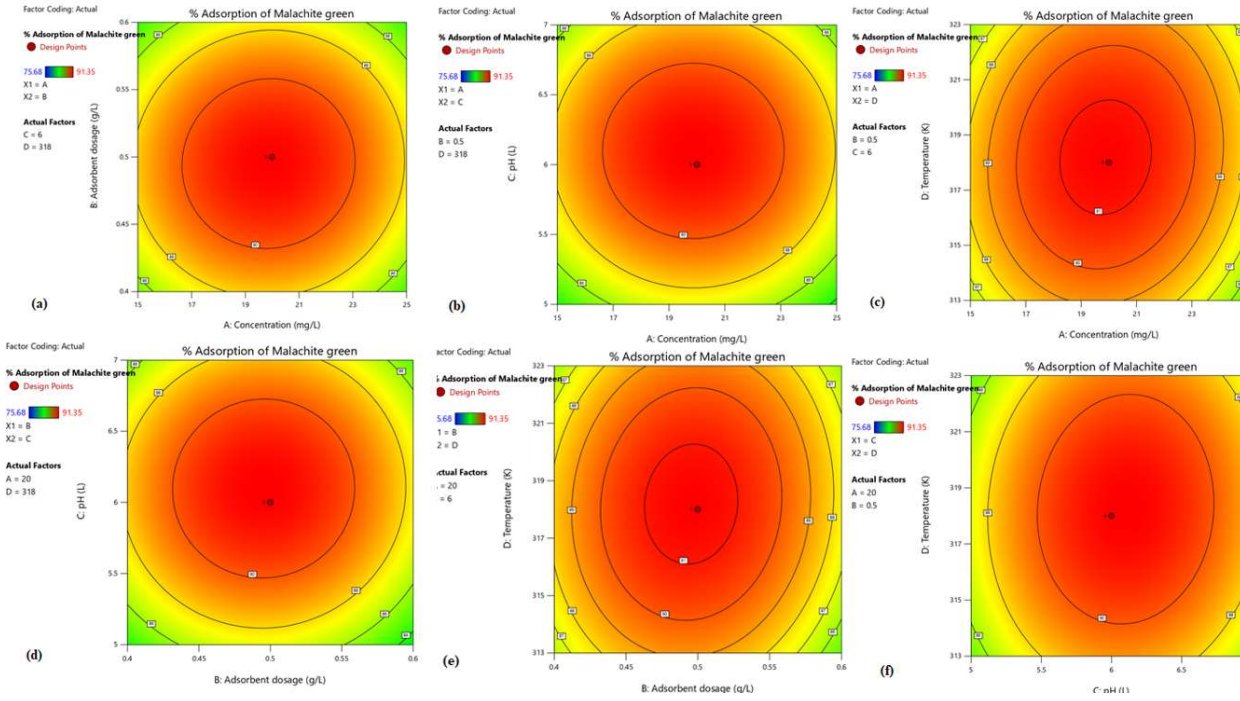

Fig. 11: 3D contour plots illustrating the interactive effects of (a) concentration and adsorbent dosage, (b) concentration and pH, (c) concentration and temperature, (d) adsorbent dosage and pH, (e) adsorbent dosage and temperature, (f) pH and temperature on the percentage removal of malachite green by TA-CuNPs.

XRD, FTIR, and Brunauer–Emmett), confirming their functional surface groups and porous morphology. In this study, TA-CuNPs exhibited efficient removal of malachite green, with adsorption strongly governed by pH, concentration, dosage, and contact time, yielding a Langmuir monolayer capacity of 243.90 $mg.g^{-1}$. The process followed pseudo-second-order kinetics and showed spontaneous endothermic behavior, with optimum batch conditions identified at pH 6 and 0.5 $g.L^{-1}$. RSM-based CCD optimization further defined the ideal operating parameters as 19.85 $mg.L^{-1}$ MG, 0.498 $g.L^{-1}$ adsorbent, pH 6.18, and 318 K, achieving the maximum removal efficiency, while the quadratic model demonstrated strong statistical validity through high R^2 and low error values. A comparative assessment of the reported adsorbents confirmed the competitive performance of the TA-CuNPs. To facilitate practical scale-up, further studies should thoroughly investigate multi-cycle regeneration, the impact of co-existing ions, breakthrough behavior under continuous flow or fixed-bed operation, and cost-benefit viability in comparison to commercial adsorbents.

5. REFERENCES

Agarwal, S., Tyagi, I., Gupta, V.K., Mashhadi, S. and Ghasemi, M., 2016. Kinetics and thermodynamics of malachite green dye removal from aqueous phase using iron nanoparticles loaded on ash. *Journal of Molecular Liquids*, 223, pp.1340-1347. [DOI]

Akar, E., Altinişik, A. and Seki, Y., 2013. Using of activated carbon produced from spent tea leaves for the removal of malachite green from aqueous solution. *Ecological Engineering*, 52, pp.19-27. [DOI]

Bashanaini, S.M., 2019. Removal of malachite green dye from aqueous solution by adsorption using modified and unmodified local agriculture waste. *Science Journal of Analytical Chemistry*, 7(2), pp.42-56. [DOI]

Bishwas, R.K., Mostofa, S., Alam, M.A. and Jahan, S.A., 2023. Removal of malachite green dye by sodium dodecyl sulfate modified bentonite clay: Kinetics, thermodynamics and isotherm modeling. *Next Nanotechnology*, 3-4, p.100021. [DOI]

Chinthalapudi, N., Kommaraju, V.V.D., Kannan, M.K., Nalluri, C.B. and Varanasi, S., 2021. Composites of cellulose nanofibers and silver nanoparticles for malachite green dye removal from water. *Carbohydrate Polymer Technologies and Applications*, 2, p.100098. [DOI]

Dastkhoon, M., Ghaedi, M., Asfaram, A., Goudarzi, A., Langroodi, S.M., Tyagi, I., Agarwal, S. and Gupta, V.K., 2015. Ultrasound assisted adsorption of malachite green dye onto ZnS-Cu-NP-AC: Equilibrium isotherms and kinetic studies – Response surface optimization. *Separation and Purification Technology*, 156(Part 2), pp.780-788. [DOI]

Eid, A.M., Fouda, A., Hassan, S.E.D., Hamza, M.F., Alharbi, N.K., Elkelish, A., Alharthi, A. and Salem, W.M., 2023. Plant-based copper oxide nanoparticles: Biosynthesis, characterization, antibacterial activity, tanning wastewater treatment, and heavy metals sorption. *Catalysts*, 13(2), p.348. [DOI]

Ejeta, B.A., Aaga, G.F., Fereja, W.M. et al., 2024. Biofabrication of highly effective and easily regenerated CuO nanoparticles as adsorbents for Congo red and malachite green removal. *Scientific Reports*, 14, p.24116. [DOI]

Gündüz, F. and Bayrak, B., 2018. Synthesis and performance of pomegranate peel-supported zero-valent iron nanoparticles for adsorption of malachite green. *Desalination and Water Treatment*, 110, pp.180-192. [DOI]

Gupta, N., Kushwah, A.K. and Chattopadhyaya, M.C., 2011. Application of potato plant wastes for the removal of methylene blue and malachite green dye from aqueous solution. *Arabian Journal of Chemistry*, (unknown volume/issue), pp.1-10. [DOI]

Hamdaouia, O., Saoudi, F., China, M. and Naffrechoux, E., 2008. Sorption of malachite green by a novel sorbent dead leaves of plane tree: Equilibrium and kinetic modeling. *Chemical Engineering Journal*, 143, pp.73-84. [DOI]

Hamed, B.H., Krishni, R.R. and Sata, S.A., 2009. A novel agricultural waste adsorbent for the removal of cationic dye from aqueous solutions. *Journal of Hazardous Materials*, 162, pp.305-311. [DOI]

Hassan, A.F., El-Naggar, G.A., Braish, A.G. et al., 2024. Utilization of synthesized copper ferrite/calcium alginate nanocomposite for adsorption and photocatalytic degradation of malachite green. *Journal of Inorganic and Organometallic Polymers and Materials*, 34, pp.190-206. [DOI]

Hussien Hamad, M.T.M., 2023. Optimization study of the adsorption of malachite green removal by MgO nano-composite, nano-bentonite and fungal immobilization on active carbon using response surface methodology and kinetic study. *Environmental Sciences Europe*, 35, p.26. [DOI]

Jain, R., Mathur, M., Sikarwar, S. and Mittal, A., 2007. Removal of the hazardous dye rhodamine B through photocatalytic and adsorption treatments. *Journal of Environmental Management*, 85, pp.956-964. [DOI]

Kumar, K.M., Mandal, B.K., Kumar, K.S., Reddy, P.S. and Sreedhar, B., 2013. Bio-based green method to synthesise palladium and iron nanoparticles using *Terminalia chebula* aqueous extract. *Spectrochimica Acta Part A: Molecular and Biomolecular Spectroscopy*, 102, pp.128-133. [DOI]

Mortazavi, K., Rajabi, H., Ansari, A., Ghaedi, M. and Dashtian, K., 2016. Preparation of silver nanoparticle loaded on activated carbon and its application for removal of malachite green from aqueous solution. *Synthesis and Reactivity in Inorganic, Metal-Organic, and Nano-Metal Chemistry*, 46(10), pp.1533-1542. [DOI]

Nadagouda, M.N., Castle, A.B., Murdock, R.C., Hussain, S.M. and Varma, R.S., 2010. In vitro biocompatibility of nanoscale zero valent iron particles (NZVI) synthesized using tea polyphenols. *Green Chemistry*, 12, pp.114-122. [DOI]

Njagi, E.C., Huang, H., Stafford, L., Genuino, H., Galindo, H.M., Collins, J.B., Hoag, G.E. and Suib, S.L., 2011. Biosynthesis of iron and silver nanoparticles at room temperature using aqueous sorghum bran extract. *Langmuir*, 27, pp.264-271. [DOI]

Philip, D., 2010. Green synthesis of gold and silver nanoparticles using Hibiscus rosa-sinensis. *Physica E: Low-dimensional Systems and Nanostructures*, 42, pp.1417-1424. [DOI]

Poiba, V.R., Sowjanya, B., King, P. and Vangalapati, M., 2023. Removal of methylene blue dye by using synthesized Grevillea robusta silver nanoparticles and optimization of experimental parameters by response surface methodology (central composite design). *Advances in Materials and Processing Technologies*, 10(4), pp.3013-3027. [DOI]

Shahwan, T., Abu Sirriah, S., Nairat, M., Boyacı, E., Eroğlu, A.E., Scott, T.B. and Hallam, K.R., 2011. Green synthesis of iron nanoparticles and their application as a Fenton-like catalyst for the degradation of aqueous cationic and anionic dyes. *Chemical Engineering Journal*, 172(1), pp.258-266. [DOI]

Sowjanya, B., King, P., Vangalapati, M. and Myneni, V.R., 2023. Copper-doped zinc oxide nanoparticles: Synthesis, characterization, and application for adsorptive removal of toxic azo dye. *International Journal of Chemical Engineering*, 2023, p.8640288. [DOI]

Turkan, A. and Huseyin, E., 2022. Adsorption of malachite green and methyl violet 2B by halloysite nanotube: Batch adsorption experiments and Box-Behnken experimental design. *Materials Chemistry and Physics*, 291, p.126612. [DOI]